Journal of Metals, Materials and Minerals, 37(2), e2752, 2027

The effects of solution nitriding and annealing on microstructure, mechanical properties, and corrosion properties of 201 J1 austenitic stainless steel

Nithi SAENARJHAN[1*], Patama VISUTTIPITUKUL[1], and Jatupon OPAPAIBOON[1]

[1] *Department of Metallurgical Engineering, Faculty of Engineering, Chulalongkorn University, Bangkok, 10330, Thailand*

***Corresponding author e-mail**: nithi.s@chula.ac.th

Received date:
25 May 2025
Revised date:
29 September 2026
Accepted date:
23 October 2026

Keywords:
Austenitic stainless steel;
Solution nitriding;
Heat treatment;
Mechanical properties;
Corrosion

Abstract

Microstructure, hardness, tensile, and corrosion properties of 201 J1 austenitic stainless steel were investigated after solution nitriding and annealing. After solution nitriding, a diffused nitrogen layer was observed near the surface along with Cr-carbides/carbonitrides at grain boundaries. The diffused nitrogen layer disappeared, while thinner high Cr martensite/austenite layers formed on the surface after the annealing of the nitrided specimen. Yield strength decreases for nitrided specimen, whereas tensile strength and elongation increase. After annealing, yield strength is further decreased, however, tensile strength and elongation also decrease as the specimen breaks before necking due to the hard martensite surface. Microhardness of the nitrided specimen slightly increased near surface and decreased at the center. For the nitrided then annealed specimen, the microhardness significantly increased at the outer martensite layer, while the increase was small at the underneath austenite layer and then reduced at the center. Corrosion properties of the nitrided specimen slightly increased due to the formation of a diffused nitrogen layer, regardless of small number of precipitates at grain boundary. On the other hand, the nitrided then annealed specimen enhances the corrosion resistance compared to the as-received condition by the formation high Cr layers and the dissolution of Cr-carbides at the surface.

1. Introduction

Austenitic stainless steel is widely used in many applications such as household objects, oil & gas tubes, etc. The advantages of austenitic stainless steel over others are its properties: high corrosion resistance, toughness, and formability [1]. Nickle (Ni) is added in high amount to counteract the effects of Chromium (Cr) and obtain a fully austenitic structure. However, Ni is one of the major reasons for its high cost. Furthermore, Ni can add complexity to austenitic stainless steels in bio-medical applications as it causes Ni poisoning when it reacts with the fluids in the human body [2].

To reduce the price while maintaining the benefit of austenitic structure, high Mn austenitic stainless steel is promoted as a high performance material. Manganese (Mn) is also an austenite stabilizer, and it is used as a substitute for Ni. Moreover, Mn not only enhances corrosion resistance of austenitic stainless steels [3] but also affects the stacking fault energy (SFE) of austenitic structure differently from Ni, thus resulting in different deformation behavior [4]. To overcome this hindrance, Nitrogen (N) is added along with Mn as a solid solution. Numerous researches reported that N increase the corrosion resistance [5], yield strength [6,7], and SFE [7] of stainless steel, thus counteracting the lack of Ni in high Mn austenitic stainless steel.

In recent days, there have been several attempts to add N into stainless steels, using various methods such as nitriding [8–13] and high temperature nitrogen absorption [14,15]. Generally, the objective of nitriding in carbon steel is to form a hard nitride layer on the surface [16]. The formation of nitride compounds in stainless steel, particularly Cr_2N, has a negative effect on corrosion resistance especially inter-granular corrosion [17]. However, there are studies presenting ways to achieve N as a solid solution atom in stainless steels via nitriding process [9,10,12,13].

The most popular nitriding process to incorporate N into austenitic stainless steels without nitride formation is low temperature plasma nitriding [10,18]. The goal is to form a layer so-called “S-phase” with highly saturated N atom, which is beneficial for austenitic stainless steels in terms of various properties [18]. However, the layer is difficult to form due to the low diffusion of N at low temperature [18]. Some studies suggest adding post-nitriding solution annealing after the nitriding process as another way to obtain solid solution of N [9,11]. As a result, solution nitriding combining with solution annealing was chosen as method for this study due to the easier operation compared to low temperature plasma nitriding. However, prior studies examining the combined effects of solution nitriding and post-nitriding annealing on high-Mn, low-Ni austenitic grades are limited and mostly done in popular grade such as 304 [9].

This present work is conducted to study the effects of solution nitriding and annealing on microstructure, mechanical properties, and corrosion properties of High Mn Austenitic Stainless Steels. AISI 201 J1 austenitic stainless steel was chosen for this study as a represent grades. The effects of treatments will be discussed based on the characterized microstructure in relation to the obtained mechanical properties, tensile and microhardness, and corrosion properties data.

2. Experimental procedure

2.1 Preparation of test specimens

The chemical composition of AISI 201 J1 austenitic stainless steel used in this study is shown in Table 1. The as-received plate was cold rolled to a thickness of 1.2 mm and then continuously annealed. The plate was cut into 3 pieces with similar dimensions for further heat treatment. One of the plates was set aside as the as-received condition. The other two plates were then subjected to a solution nitriding process at 1050°C, with the heating profile shown in Figure 1(a). Specimens were heated slowly under vacuum (<5 Pa) to 950°C then 1050°C followed by the introduction of nitrogen gas for solution nitriding. Cooling was conducted under vacuum (<5 Pa) to 950°C, then under pressurized nitrogen gas to 60°C to avoid distortion. After nitriding, one of the plates was then annealed at 1200°C with 10°C·min^{-1} heating rate in a vacuum atmosphere for 60 min and cooled with pressurized nitrogen gas down to 50°C (Figure 1(b)).

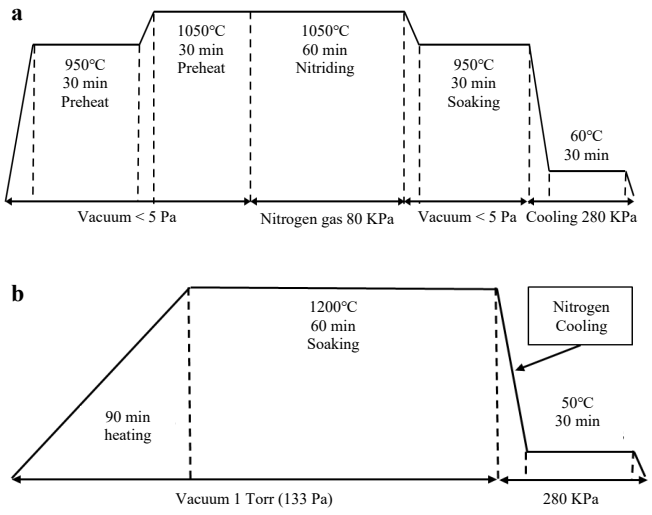

Figure 1. Heat treatment profiles of (a) solution nitriding, and (b) annealing after solution nitrided.

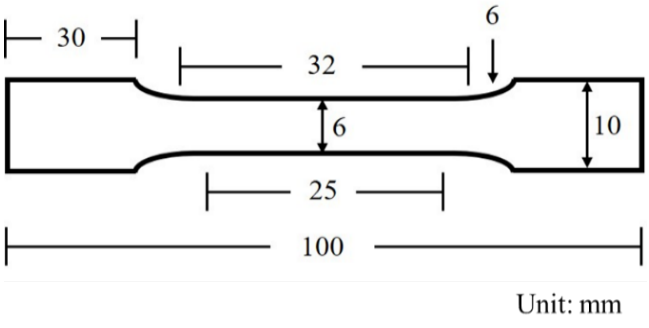

Figure 2. Flat shape sub-size tensile specimen according to ASTM E-8 standard.

After heat treatment, 3 groups of specimens were obtained: as-received (AR), solution nitride (SN), and solution nitride then annealed (SNAN). To study the microstructure, small pieces of specimens were cut from all groups along the rolling direction. These pieces were mechanically grounded in cross-section with sandpaper from 80 grid to 2000 grid, then polished with 1 µm diamond paste and electrochemically etched with a 10 vol% oxalic acid solution.

2.2 Microstructure observation

The Optical microscope (OM) was used to observe the overall cross-sectional microstructure of all groups of specimens. To further characterize the details of the microstructure, Scanning electron microscope (SEM, JEOL, model JXA-ISP100), equipped with Wavelength dispersive spectroscopy (WDS, JEOL, model EX-74500U4L2X) and Electron probe micro-analyzer (EPMA, JEOL, model JXA-iSP100 super probe) was utilized. Phases were distinguished using X-ray diffractometer (XRD) with Cu-source operated on the surface of the specimens. In addition to the data acquired from surface, the nitrided specimens and those nitrided and then annealed specimens were also grounded to obtain the data from the beneath layers.

2.3 Measurement of mechanical properties

For mechanical properties, tensile and hardness properties were tested in this study. Sub-size tensile specimens were cut from the plates after heat treated according to the ASTM-E8 standard (Figure 2). The tensile test was conducted with a constant crosshead speed of 1.5 mm·min^{-1} until fracture.

Micro-Vickers and Nanoindentation tests were performed to evaluate cross-section hardness using the same etched specimens after microstructure characterized. The micro-Vickers test was conducted using a load of 10 g to study the hardness in each area of the specimens in each group. Nanoindentation was performed using a force of 50 mN and 100 mN for thin layer and diffused layer, respectively, with 20 s of force increase rate and creep for 5 s then lastly, reducing force with the similar rate of increasing. The experiment was done to obtain localized properties, such as hardness and elastic modulus, in smaller areas, especially in the layers at the surface, of the heat-treated specimens.

2.4 Measurement of corrosion properties

Lastly, corrosion properties were tested using a Metrohm PGSTAT 302N Potentiostat/Galvanostat with three-electrode cells containing 180 cm^3 of 3.5 wt% NaCl solution. The solution of 3.5% was selected as substitute for sea water which is a general atmosphere for stainless steels applications. Hence, the comparison between 201J1 and other stainless steel grades can be made. All tests were conducted at room temperature using an Ag/AgCl electrode as a reference electrode (RE).

Table 1. Chemical composition of 201 J1 specimen in this study.

Chemical composition [wt%]										
Fe	**C**	**Si**	**Mn**	**Cr**	**Ni**	**Co**	**Cu**	**N**	**P**	**S**
Balanced	0.095	0.419	9.979	13.820	1.027	0.150	1.182	0.146	0.039	0.005

A platinum rod served as a counter electrode (CE), and the specimen, with an exposed surface area of 1.0 cm^2, was employed as a working electrode (WE). To determine open circuit potential (OCP), specimens were immersed in the solution for 1200 s. After OCP, potentiodynamic polarization was performed at –500 mV with respect to the OCP values and finished at +1200 mV or current limitation (10^{-2} A·cm^{-2}). Both step potential and scan rate were 1 mV and 1 mV·s^{-1}, respectively. Corrosion potential (Ecorr), corrosion current density (I_{corr}), Tafel's constant (β_a, β_c) and polarization resistance (R_p) were calculated using Tafel's extrapolation. To check reproducibility, at least 2 specimens were used for the corrosion tests. The range of standard deviations for potentiodynamic polarization was found to be less than 1×10^{-15}.

3. Results and discussion

3.1 Microstructure observations

3.1.1 Optical micrographs

The cross-section microstructure of the AR condition (Figure 3(a)) showed equiaxed austenite grains with a grain size around 5 μm to 20 μm in all areas. After solution nitriding (Figure 3(b)), mainly austenite was observed, and the grain boundaries near the surface area showed significant corrosion with many small pits from the etching. Furthermore, the austenite grains became significantly larger. Comparing the near surface area (to the depth where the grain boundary corrosion disappears) and the center area, the grain size near the surface was significantly smaller (20 μm to 100 μm near surface vs. more than 100 μm in the center area). The distance from the surface to where the grain boundary corrosion ended represents the depth of the diffusion layer (approximately 300 μm) obtained from solution nitriding. The pits at the grain boundaries are likely to be caused by the formation of Cr-carbides or Cr-nitrides, which result in Cr-depletion zone.

Annealing after solution nitride results in the formation of surface layers and further grain growth in all areas (Figure 3(c)). Interestingly, the surface appears to consist of two distinct layers, top and bottom, and inside the large austenite grains, thin slip lines can be observed. These slip lines could be either mechanical twins, ε-martensite, or α′-martensite formed during the specimen preparation step such as grinding. This suggests that the mechanical stability of the austenite in the SNAN specimen is lower than that of both the AR and SN conditions. However, further characterization details are needed to confirm the identity of the surface layers and slip lines.

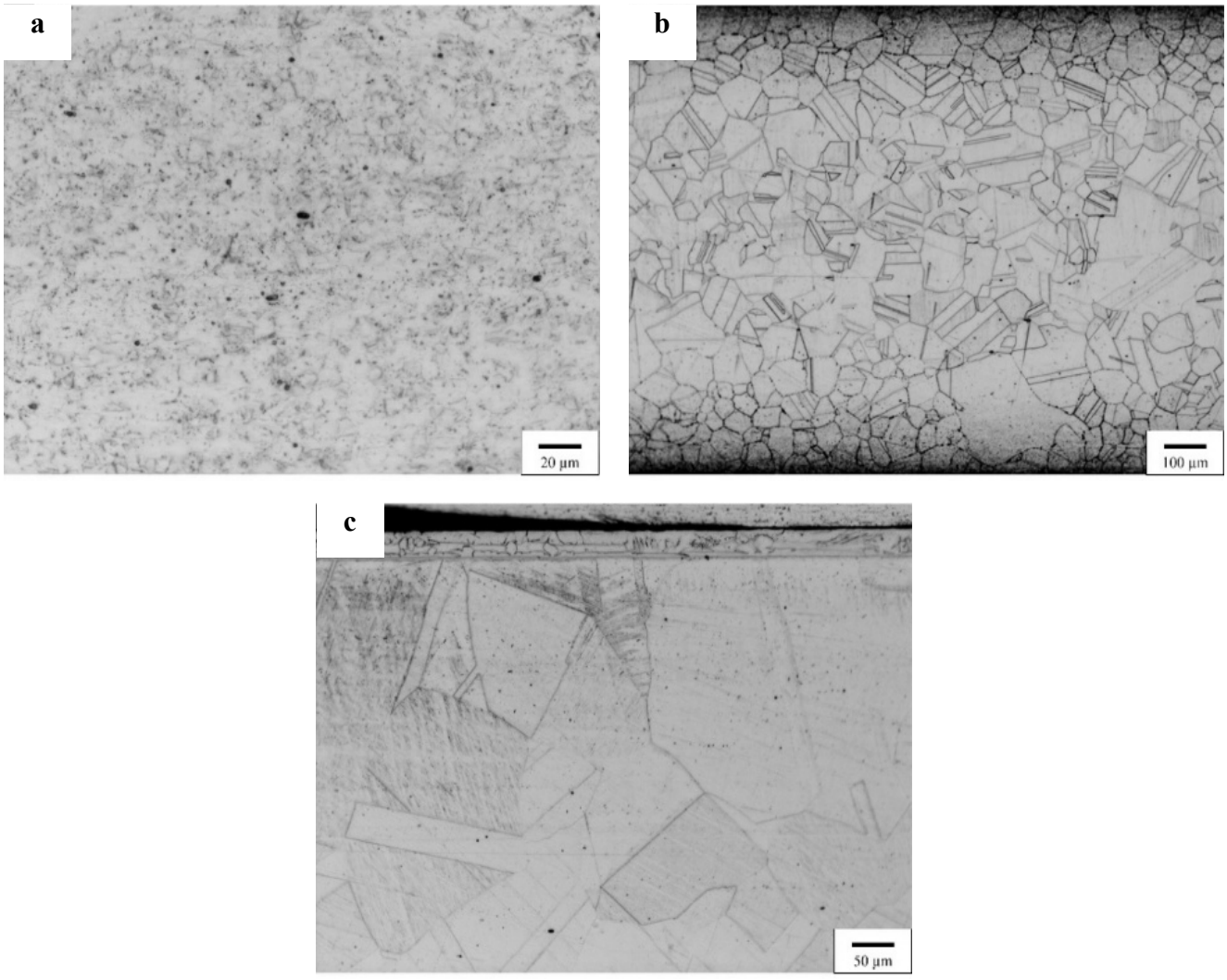

Figure 3. Optical micrographs of (a) as-received, (b) SN, and (c) SNAN specimens.

3.1.2 SEM micrographs and element distribution

The microstructure near the surface of all conditions obtained from SEM, WDS line scan, and EPMA data are shown in Figure 4–8. For the AR specimen (Figure 4), only small austenite grains were presented, and no specific partitioning of any element was found in the whole area. Near surface of the SN specimen, Figure 5, showed austenite grains with many pits around the grain boundary. These pits exhibit a high concentration of C with some traces of N, while Cr is reduced mainly at the large pits along with the lack of Fe around the pits. These suggest that chromium carbide, nitride, or carbonitride particles are likely formed after nitriding at the grain boundary, and the Cr rich particles fall off during etching. According to previous studies [19–23], the typical types of carbide, nitride and carbonitride particles in austenitic stainless steels are Cr-rich particles such as $Cr_{23}C_6$, Cr_7C_3, Cr_3C_2 [20,21], Cr_2N [22], and $Cr_2(CN)$ [23], with $Cr_{23}C_6$ being the most frequently observed type in stainless steel [19]. Thus, the observed precipitates are likely $Cr_{23}C_6$ and $Cr_2(CN)$ as the most probable phases. Moreover, the EPMA data also confirms the diffusion layer of N which shows small gradient of N from the surface, reducing along the thickness until reaching a constant value after 300 µm. In addition, WDS line scan (Figure 6) displays the highest gradient of N around 50 µm from the surface, and a high C content at the grain boundaries.

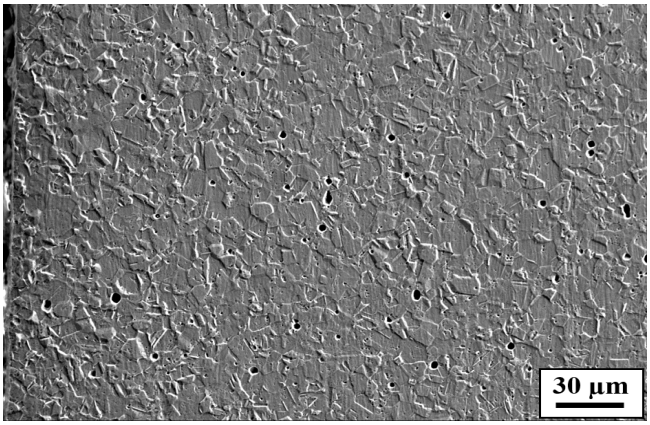

Figure 4. SEM micrographs of as-received specimen.

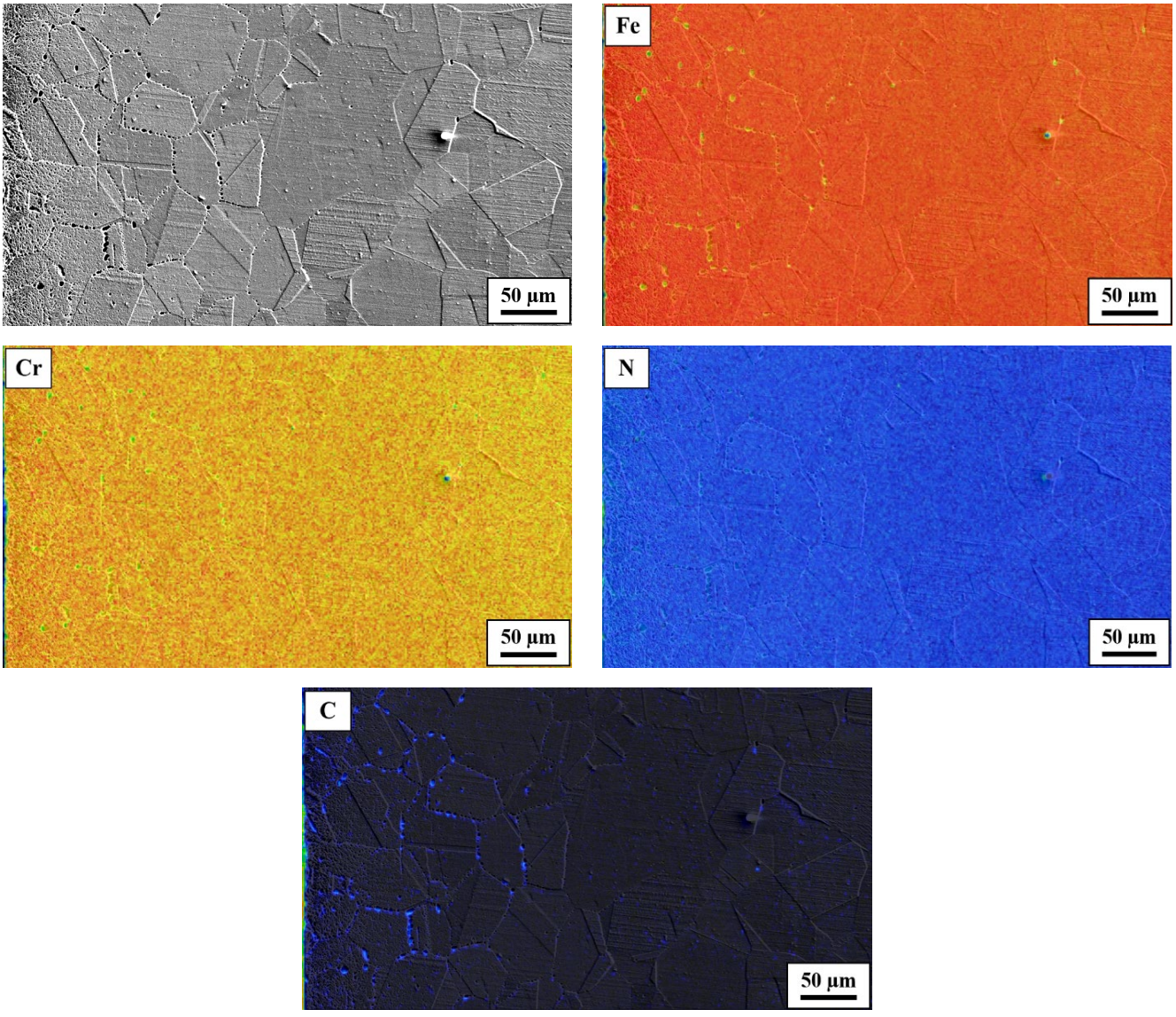

Figure 5. SEM micrographs of SN specimen and Fe, Cr, C, and N distribution maps.

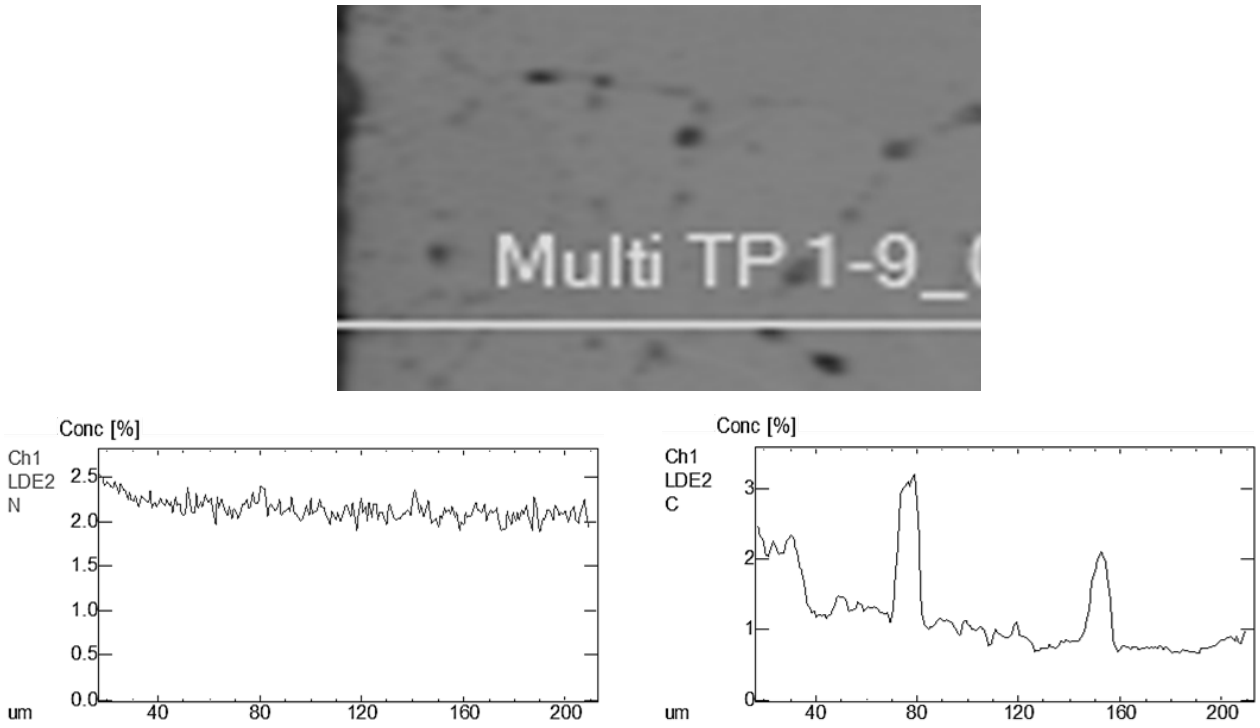

Figure 6. WDS line scan of N and C near surface of SN specimen.

For the SNAN specimen in Figure 7, pits at austenite grain boundary disappeared. Instead, large austenite grains with slip lines in the grain interior and the surface layers were found. The microstructure at the surface shows two distinct morphologies from two layers, with a grainier at the top and more elongated at the bottom. The combination of the two layers is 20 µm to 30 µm. This implies that most of the Cr-carbides were dissolved, the diffusion layer of N disappeared, a layer with 2 distinct morphologies formed after annealing at 1200°C in a vacuum.

According to EMPA (Figure 7) and WDS line scan (Figure 8) results, both layers have majorly similar chemical composition despite different appearance. The layers are significantly higher in Fe and Cr, slightly higher in Si, Ni, N, and C but lower in Mn (though not significant in WDS line scan) compared to the austenite grains underneath. The N distribution in surface layers (Figure 7) shows slightly higher concentration at the top layer compared to the bottom layer which can result in the difference between these two layer. Furthermore, N concentration underneath the layers is lower compared with diffusion layer in SN specimen and homogeneous. Thus, by annealing after solution nitriding, N is more concentrated in the layers, and a homogeneous distribution of N inside was achieved; nonetheless, the identity of the surface layers still needs to be investigated.

3.1.3 Phase identification

XRD data from SN and SNAN conditions are shown in Figure 9. After solution nitriding (Figure 9(a)), mainly BCC and FCC peaks were observed at the surface. FCC peaks represent the austenite matrix, while BCC peaks could correspond to α′-martensite, as it has BCT structure mixed with Cr-carbides. This is unexpected since the micrographs, OM (Figure 3(b)) and SEM (Figure 5), do not show any martensite at the surface. Nonetheless, severe corrosion was observed after etching at the top 30 µm of the surface, where the lack of C in austenite grain is presumed to be due to the formation of carbides. This leads to a decrease in austenite stability [7,24,25] and possibly cause a martensitic transformation at the top surface during cooling from nitriding temperature. After grinding out around 100 µm from the surface, mainly FCC austenite peaks with very weak intensity of α′ peak were observed which agrees with the micrographs results.

After the annealing of solution nitride specimen, FCC and BCC peaks were observed at the surface. The appearance of BCC peaks suggests that either BCC-ferrite or BCT-martensite is present in the surface layers. After grinding down by 10 µm and 30 µm, FCC peaks diminished and mainly BCC peaks were detected. According to the microstructure, large austenite grains were the only phase observed underneath 30 µm. This suggests that FCC to BCC transformation occurred during grinding of the This emphasizes that austenite phase after annealing is highly unstable and transformed into martensite during mechanical grinding. The reason is likely to be the decrease in austenite stability as the grain size increases [26,27] and the decrease in overall nitrogen content after annealing compared to the SN specimen, as nitrogen has been reported to increase austenite stability [7,24,25].

As for the surface layer, the layer consists of at least one BCC or BCT structure, as shown in the XRD result (Figure 9). According to the micrographs (Figure 7), the layer can be separated into top and bottom layers with 2 distinctive morphologies. The element distribution (Figure 7–8) is relatively similar for both layers with small differences, where the chemical composition measurement is unlikely to be ferrite due to the high Mn content. Thus, the surface layers are likely to be α′-martensite with a BCT structure. Nevertheless, it is still unclear whether top or bottom layer with different morphologies is both α′-martensite or not. Hence, micro-Vickers and nanoindentation tests were done to obtain more details on the surface layers.

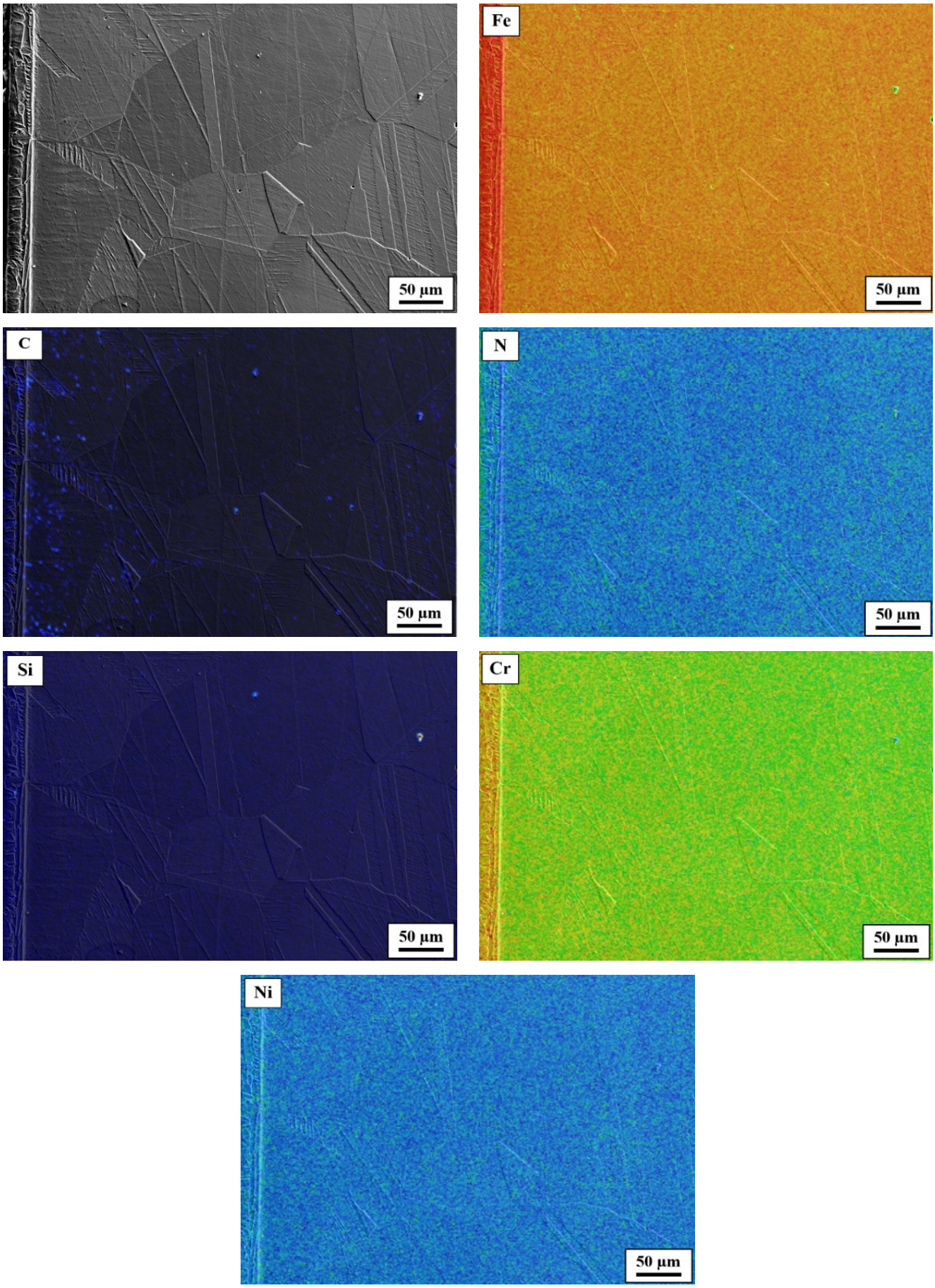

Figure 7. SEM micrographs of SNAN specimen and element distribution maps

Furthermore, it is important to understand the formation of the surface layers after annealing at 1200°C in a vacuum of the SNAN specimen. From a previous study [28], solution annealing of high N austenitic stainless steel leads to the formation of surface layers where the top layer is ferrite and the bottom layer is austenite due to the outward and inward diffusion of N. Furthermore, the outward diffusion of Mn and N was also reported during annealing at 1100°C of high Mn duplex stainless steel [29]. This suggests that during annealing, the surface layers form owing to the diffusion of alloying elements. For this instance, the relative decrease in austenite stabilizers, N and Mn, compared to ferrite stabilizer, Cr, was observed at the surface layers of the SNAN specimen (Figure 7). Since the chemical composition of the surface layers in the SNAN specimen is still austenite, it presents relatively lower stability. Thus, owing to the fast cooling caused by N gas, the top surface layer transforms into α′-martensite, while the bottom layer is still austenite due to the temperature gradient.

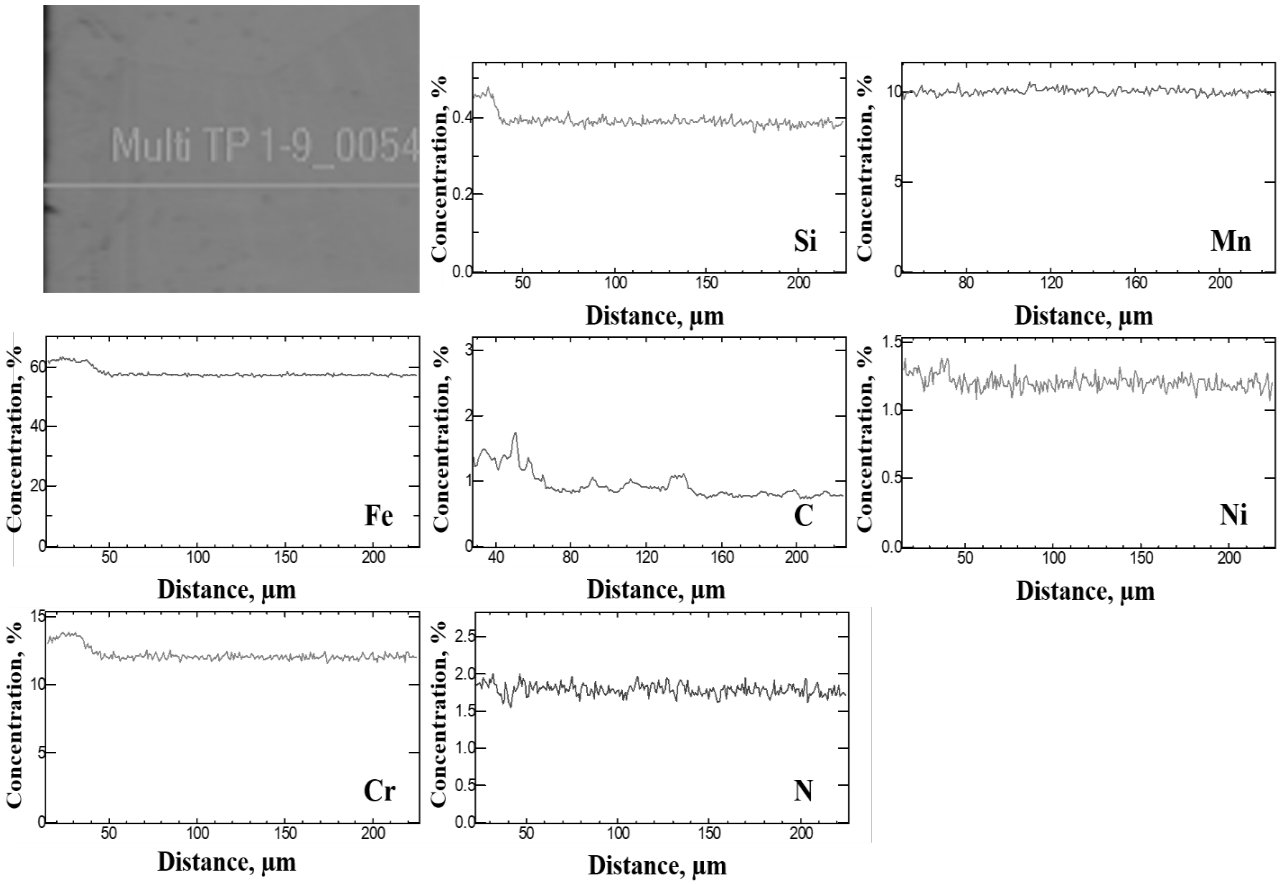

Figure 8. WDS line scan of elements near surface of SNAN specimen.

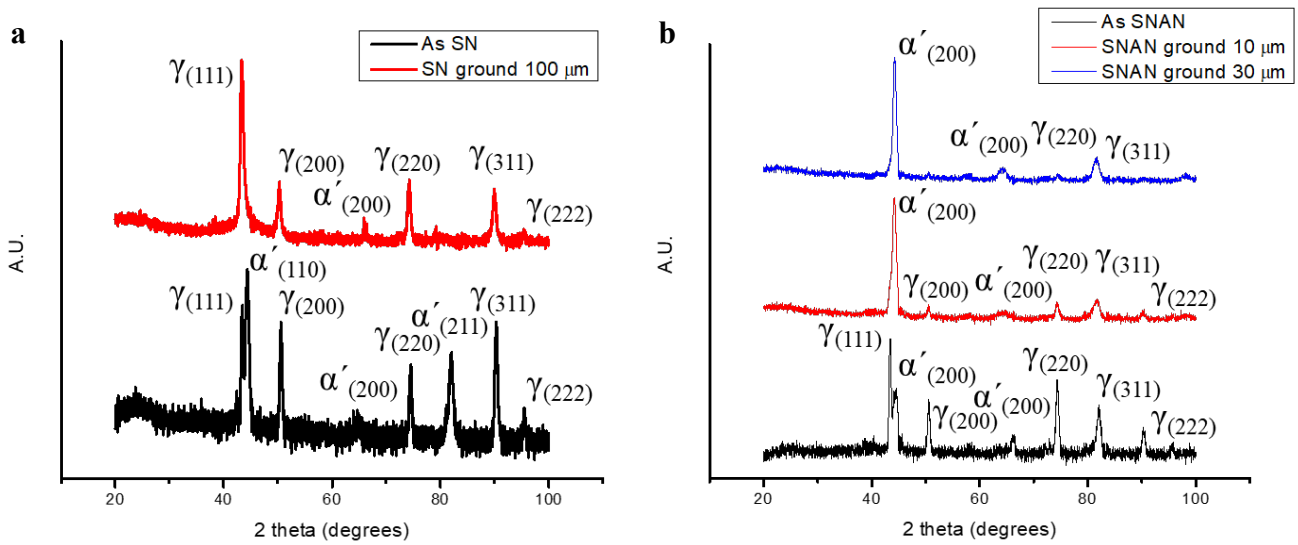

Figure 9. XRD results of (a) SN and (b) SNAN specimens.

3.2 Mechanical properties

3.2.1 Tensile behavior

The engineering stress-strain curves and the average values are displayed in Figure 10 and Table 2, respectively. The AR specimen shows the highest yield and tensile strengths of all condition, while its elongation falls between those of the SN and SNAN specimens. After solution nitriding, the yield and tensile strengths decrease, while elongation increases. The addition of annealing process after nitriding results in a further decrease in yield strength, as well as the reduction in tensile strength and elongation. However, it is important to notice a sharp drop in stress at failure, seen before necking in the SNAN specimen, indicating the brittleness of this specimen's condition. This causes the specimens to break before reaching their highest potential, thus reducing the average values of tensile strength and elongation. Furthermore, there is a sudden increase of stress values during deformation, which is typical of the character of TRIP effect [30] in the AR and SNAN conditions.

To observe the work hardening behavior, the true stress-strain curves along with the strain hardening rate were plotted (Figure 11). The overall results follow a similar trend to the engineering stress-strain curve with an enhanced difference of SNAN condition apart from other conditions. All specimens show a rapid drop in strain hardening rate immediately after plastic deformation started. Nevertheless, for the AR and SNAN conditions, the strain hardening rate increases after a certain degree of plastic deformation, but the increase is less intense for the AR specimen. In the AR specimen, after the strain hardening rate reaches a plateau, it gradually decreases with increasing strain and drops to zero just before failure. In contrast, the strain hardening rate of the SNAN specimen reduces to zero rapidly before or immediately after the plateau which indicates the brittle behavior. Moreover, for the SN condition, the strain hardening rate steadily decreases during plastic deformation before failure, which is completely different from the other conditions.

The significant increase in strain hardening rate during plastic deformation for the AR and SNAN conditions is typical of the TRIP effect in austenitic steels [30] and consistent with the phase analysis from XRD after grinding the SNAN condition, as shown in Figure 9(b). The discrepancy in strain hardening rate between two conditions during straining is likely due to the difference in austenite stability, where austenite in AR is more stable. As for the SN specimen, the TRIP effect is unlikely as also indicated by the absence of martensite peaks after grinding (Figure 9(a)). Nonetheless, the strain hardening rate is almost constant, with only a very gentle decrease throughout the plastic deformation process, resulting in the highest elongation of all condition. This suggests that deformation mechanisms such as TWIP [31,32] or even Microband-Induced Plasticity [33] occur during straining, as these mechanisms enhance strain hardening behavior and elongation in austenitic steels. The absence of TRIP behavior in the SN specimen is caused by the increase in N concentration in the N-diffused layer, where N can significantly enhance mechanical stability of the austenite phase [7,24,25].

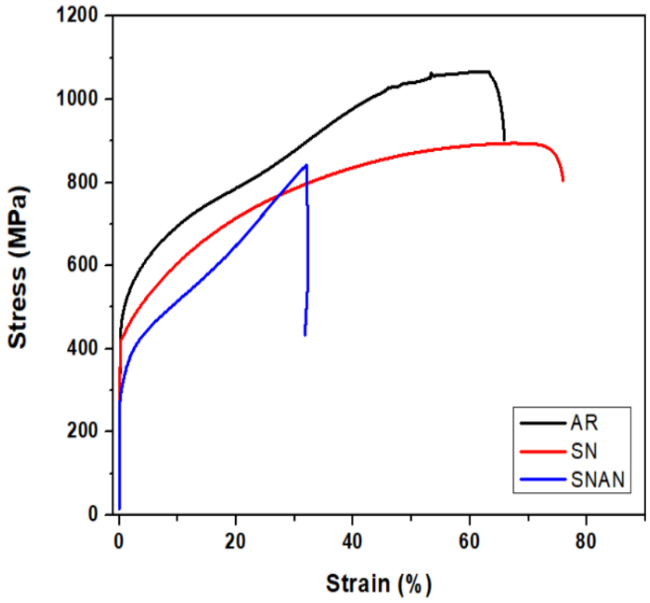

Figure 10. Engineering stress-strain curves of AR, SN, and SNAN specimens.

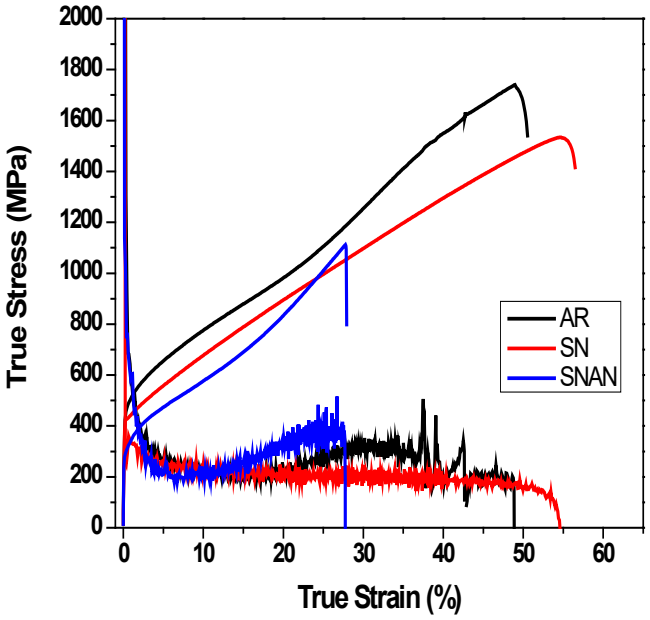

Figure 11. True stress-strain curves and strain hardening rate of AR, SN, and SNAN specimens.

Table 2. Yield strength, tensile strength, and elongation at failure of the AR, SN, and SNAN specimens.

Specimen	Yield strength [MPa]	Tensile strength [MP]	Elongation at failure [%]
AR	464.01 ± 2.45	1071.08 ± 4.47	66.18 ± 0.74
SN	423.06 ± 0.55	896.30 ± 2.13	75.55 ± 0.55
SNAN	292.41 ± 1.23	882.74 ± 70.68	35.78 ± 5.83

3.2.2 Hardness properties

From Table 3, the average hardness of the AR specimens is 285 HV, and the values are consistent across the specimen. On the other hand, the SN and SNAN conditions exhibit a decrease of hardness from the surface to the center of the specimens, as seen in Figure 12. For the SN specimen, the hardness drops relatively quickly as the area moves below the surface and remains steady in most areas. However, the difference between the maximum hardness at the surface and the minimum hardness is small, 96 HV. The average hardness values near the surface are 307 HV and 317 HV for both side of the specimen, while the average value of the center area is 252 HV. This suggests the presence of layer at the surface, and its properties are not significantly different from the original material, which is consistent with the observed microstructure (Figure 3(b)). Compared to AR, the hardness near surface is increased which aligns with the observation of N diffused layer whereas, the hardness at the center reduced due to the decrease in residual stress and larger grain size from solution nitriding process.

In the case of the SNAN specimen, the hardness value decreases as the distance from the surface increases for both sides. The decrease is significant, from the highest of 580 HV (for the outset layer) to the lowest value of 221 HV (for the center area). The high value is significantly higher than any values in other conditions while the low value is also the lowest for all conditions. This suggests that hard layer was formed at the surface and the further increase in grain size with very low residual stress results in low hardness in the center. According to the observed microstructure (Figure 3(c)), two layers with distinct appearance were found. The average hardness values were taken from both layers, the interlayer beneath, and the center area. The average hardness values at the outer surface layer are 556 HV and 484 HV, while the average hardness values for the layer beneath are 375 HV and 384 HV for both side of the specimen. On the other hand, the interlayer and center area have low hardness values and are relatively similar, with average hardness value of 285 HV and 247 HV, respectively. This indicates that the two distinct layers formed in the SNAN specimen have different properties, regardless of similar element distribution (Figure 7), and the layers in the SNAN specimen are different from the SN condition.

Furthermore, nanoindentation was performed to obtain more details on the hardness and elastic modulus distributions of the layers of the SN and SNAN specimens and the results are shown in Figure 13–14. In these figures the distance between each measuring point was 30 μm in each axis. For the SN specimen, the hardness values in the diffuse layer (Figure 13(a)) are evenly distributed around 300 HV inside austenite grains. However, some spots, particularly at the grain boundaries, show slightly higher hardness, reaching up to 370 HV, due to the presence of small particles. Moreover, the elastic modulus, ranging around 220 GPa, demonstrate a trend well aligned with even distribution of hardness values. The results agree with previous hardness measurement conducted with higher load.

As for the SNAN specimen, the hardness distribution extends from the surface to a similar depth as the SN specimen (Figure 14(a)). The results show some high hardness values, above 400 HV, arrange at the surface area, while most values are evenly distributed at around 300 HV in other areas. The hardness values obtained from nanoindentation are somewhat higher than from micro-Vickers measurement however, the distribution tendency is equivalent. On the other hand, the elastic modulus, approximately 210 GPa, remains consistent throughout the specimens. More details of the layer in the SNAN specimen are shown in Figure 15. The hardness values in the surface layer are significantly higher than those in other areas, ranging from 460 HV to 730 HV. As the depth increases, hardness decreases to its lowest point just beneath the layer, mostly below 400 HV, then slightly increases with further increase depth to around 480 HV. This indicates the presence of 3 different characters existing near the surface of the SNAN specimen. Furthermore, the elastic modulus distribution follows the opposite trend to hardness, where the surface layer area exhibits lower values compared to other areas, and then increases with more depth. It is to be noted that each measuring point for layers properties was separated by 10 μm.

Comparing the SN and SNAN results measured at the diffuse layer depth (Figure 13–14 respectively), the hardness and elastic modulus of the SN specimen are slightly higher than the SNAN specimen, which is consistent with the micro-Vickers measurement, even though the difference is lower. This is due to the higher N content throughout the diffuse layer of the SN specimen compared to the SNAN as the solid solution of N has been reported to increase strength [6,7], hardness [11,12], and elastic modulus [34] of austenitic stainless steels.

The high hardness at the outer surface layers of the SNAN specimen cannot be considered as nitride layer, so-called “white layer”, since the hardness is not as high [8,9,11]. According to the XRD result, a BCC structure was found on the surface of the SNAN specimen. Thus, combining its high hardness with the chemical composition (Figure 7), the outer surface layer is considered to be α′-martensite. As the measured depth increases toward the bottom layer, the hardness significantly decreases, indicating a change in mechanical properties. Since the chemical composition is not suitable to be ferrite, the low hardness bottom layer is likely austenite. However, due to fluctuation in the martensite layer thickness and the variation in alloying element distribution (Figure 7), these factors affect the hardness of austenite near the surface, resulting in a higher hardness than the average values compared to austenite grains inside. Additionally, the difference in elastic modulus between martensite and austenite layers could originate from the difference in crystal structure [35], alloying element distribution [35,36], and stress [37].

Table 3. Micro-Vickers hardness of the AR, SN and, SN+AN specimens.

Specimen	Hardness [HV]			
	Surface	Center	Interlayer	Underlayer
AR	282.42 ± 12.26	287.04 ± 16.00	-	-
SN	311.89 ± 14.20	251.86 ± 15.98	-	-
SNAN	550.48 ± 15.41	247.18 ± 15.21	454.11 ± 22.62	279.17 ± 14.87

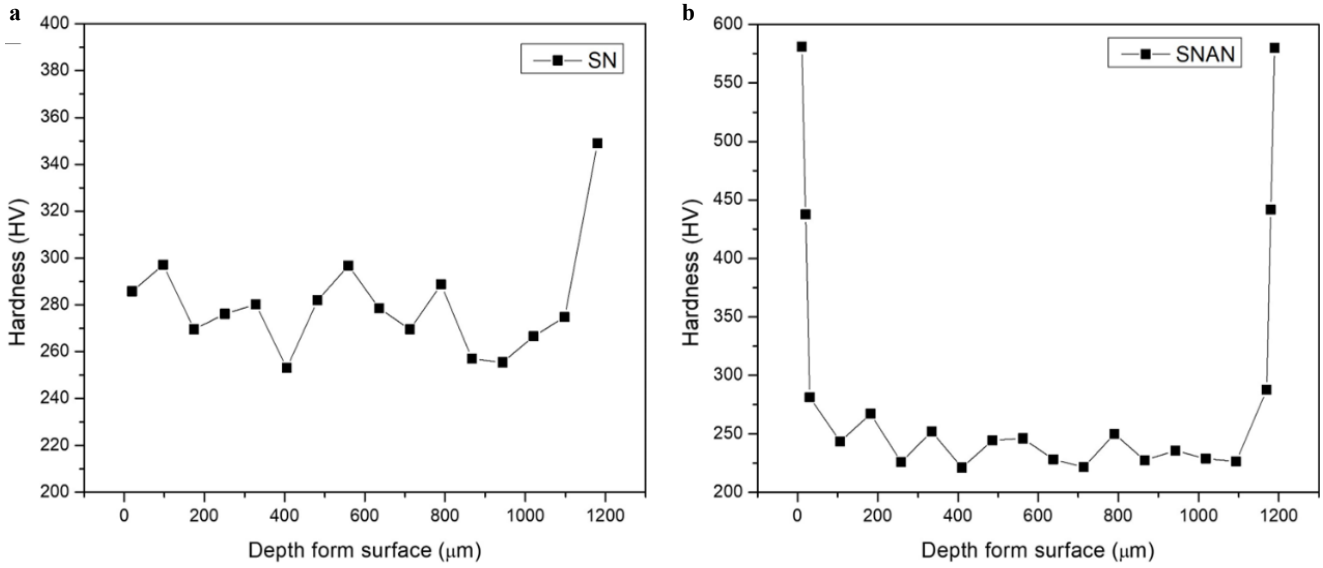

Figure 12. Micro-Vickers hardness profile of SN and SNAN specimens.

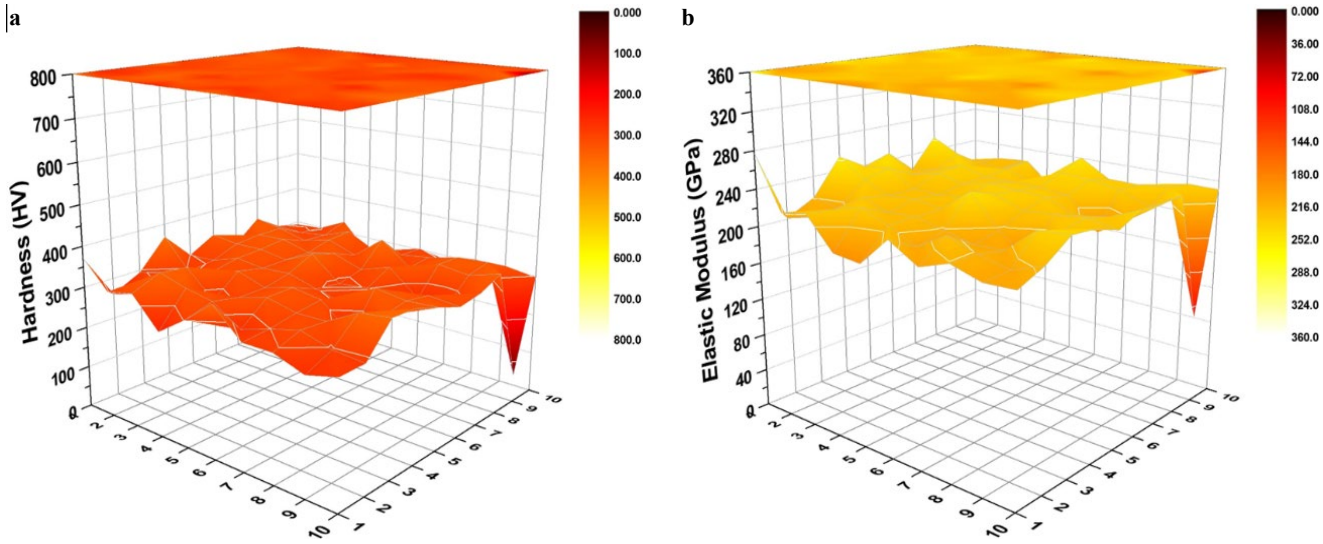

Figure 13. Hardness and elastic modulus profiles at the diffused layer of SN specimen.

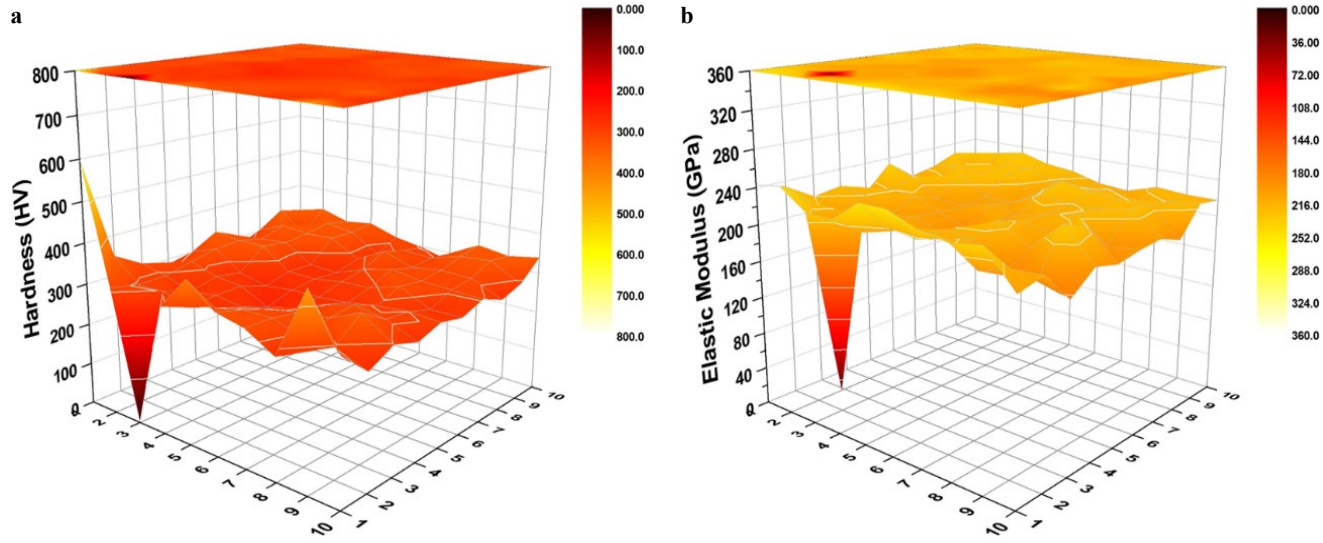

Figure 14. Hardness and elastic modulus profiles at the diffused layer of SNAN specimen.

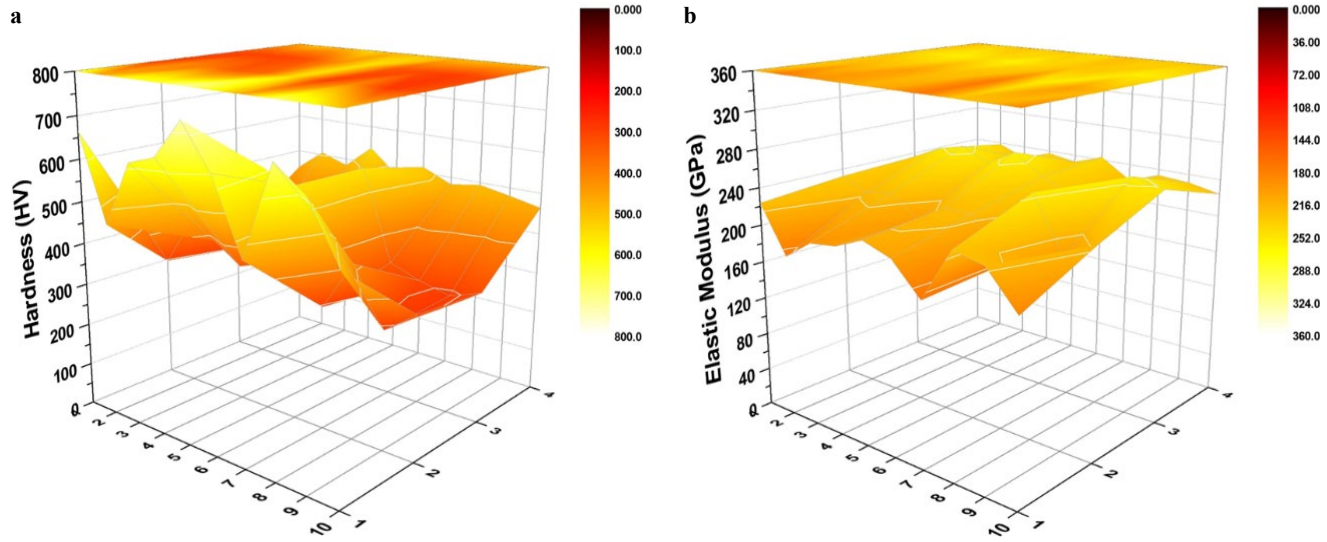

Figure 15. Hardness and elastic modulus profiles at the surface layer of SNAN specimen.

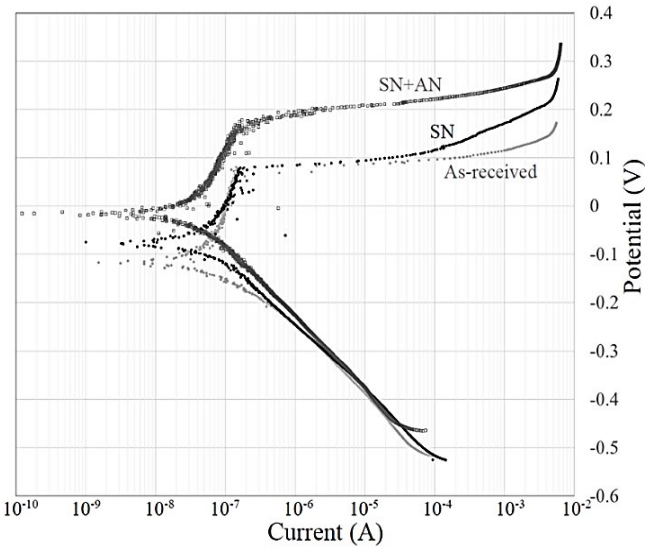

Figure 16. The potentiodynamic polarization test results for AR, SN, and SNAN specimens.

3.3 Corrosion properties

The potentiodynamic polarization tests for the AR, SN, and SNAN specimens are presented in Figure 16. From the results, the corrosion potential (E_{corr}) of the SNAN specimens is –0.02 V which is the highest compared to the SN and AR specimens, E_{corr} = –0.06 V, and –0.12 V, respectively. The corrosion current (I_{corr}) for all groups is similar, within the range of 10 A·cm^{-2} to 8 A·cm^{-2}, suggesting comparable corrosion rates although slightly, SNAN specimen shows the lowest I_{corr} followed by SN and AR specimens respectively. As a result, the overall corrosion resistance of 201 J1 austenitic stainless steel is enhanced by solution nitriding and further improved by annealing after being solution nitrided.

Furthermore, based on the potentiodynamic polarization test results, all specimens exhibit passivation behavior, with passive current in the range of 10^{-7} A·cm^{-2}. Notably, the SNAN specimens demonstrate the highest breakdown potential at 0.18 V, while the SN and AR specimens exhibit lower potential of 0.12 V and 0.08 V, respectively. The increased breakdown potential of the SNAN and SN specimens, compared to AR specimens, is believed to be related to the microstructure described in section 3.1 and will be further discussed in section 3.4.2.

3.4 Relationship between microstructure and properties

3.4.1 Microstructure and mechanical properties

According to the microstructure and mechanical properties results, the AR specimen shows a fully austenitic structure with a small grain size, the highest yield and tensile stresses of all conditions, TRIP behavior, moderate elongation, and low hardness values across all areas. The high yield stress is due to the small grain size, while the high tensile stress and moderate elongation results from the occurrence of TRIP behavior during deformation. This suggests that the austenite phase in 201 J1 stainless steel is not mechanically stable and transforms to martensite via plastic deformation, regardless of small grain size. The results are consistent with previous observation on others high Mn stainless steels [38,39]. However, the low hardness values indicate that martensitic transformation does not occur in the early stage of deformation, which is beneficial for its mechanical properties.

In case of the SN condition, large austenite grains, N-diffused layer of approximately 300 μm from the surface, martensite layer at the surface, and the Cr carbide/carbonitride particles at grain boundary inside N-diffused layer were observed. Moreover, the SN specimen has lower yield and tensile stresses, but higher elongation compared to the AR specimen without noticeable TRIP behavior. The decrease in strengths is related to the significant increase in grain size and the absence of martensitic transformation, as confirmed by XRD. However, the improvement in elongation is attributed to another deformation mechanism such as TWIP [31,32] of Microband-Induced Plasticity [33] instead. The results indicate that the mechanical stability of the austenite phase increases after solution nitriding due to the small increase of N content. As for hardness, there is a noticeable increase hardness in diffusion layer compared to AR specimen due to the presence of N diffusion layer then decreases to lower values as the measured

depth goes below 300 μm from the surface due to the increase grain size and lower residual stress. Noticeably, high hardness spots at grain boundaries confirm the presence Cr carbide/carbonitride particles. Nevertheless, small appearance of martensite at the surface, as detected via XRD, did not affect hardness as typical martensite due to the lack of solute C atom as suggested in the previous study [40].

In the SNAN specimen, the N-diffused layer disappeared and the martensite/austenite layer with two distinct features is observed on top of a large austenite grain. Meanwhile, the yield and tensile stresses, as well as elongation, are the lowest among the three conditions despite the most extreme work hardening from TRIP behavior. The decrease in yield stress is mainly due to the growth of austenite grain after heat treatment. In contrast, the lowest tensile strength and elongation is caused by the presence of brittle martensite layer at the surface, which forms crack easily during plastic deformation resulting in brittle failure behavior. Additionally, the highest work hardening rate implies that the mechanical stability of austenite is the lowest in the SNAN condition, which is consistent with the microstructure observation due to the largest grain size and the decrease in austenite stabilizer content. Lastly, the hardness values of the martensite/austenite layer exhibit greater hardness in the martensite upper region and low hardness in the austenite lower region. The hardness of martensite layer in the SNAN specimen is higher than that of the SN specimen owing to the difference in amount of martensite detected via XRD (Figure 9) and chemical composition [40], which originated from the dissolution of carbide/carbonitride particles and element partitioning during annealing. Furthermore, the large austenite grain inside shows the lowest hardness due to the large grain size and low residual stress, which explains the observed lowest yield stress compared to other conditions.

3.4.2 Microstructure and corrosion properties

According to the microstructure observation and EPMA analysis (section 3.1), the SNAN specimen processes a high-Cr layer up to 30 μm in thickness on the surface. This high-Cr layer acts as a protective layer, thus an increase in corrosion potential (E_{corr}) and breakdown potential compared to the AR and SN specimens was observed (Figure 16). This is consistent with the previous studies that higher Cr content leads to better corrosion resistance of stainless steels [41,42]. Along with Cr, N was also found near the surface of SNAN specimen (Figure 7) this is also beneficial for corrosion resistance [8]. For the SN specimens, a high-nitrogen content layer was detected with evenly distributed chromium content although comparatively lower than the SNAN specimens. This nitrogen diffusion layer provides a beneficial result on corrosion resistance. However, high Cr precipitates inside diffusion layer have negative influence on corrosion resistance [8,42]. Thus, SN specimen shows less impact on the corrosion protection compared to the SNAN specimens.

The corrosion test results indicate that introducing nitrogen into 201 J1 austenitic stainless steel via solution nitriding forms a high-nitrogen content layer with some precipitation of Cr-carbides/carbonitrides at grain boundary, which enhances of corrosion resistance by increasing both the corrosion and breakdown potentials. By annealing SN specimens (SNAN specimens), the corrosion resistance is further enhanced due to the dissolution of Cr-carbides/carbonitrides and the formation of Cr-rich layer on the surface. This layer acts as an effective protective barrier, which is crucial for achieving enhanced corrosion resistance in the SNAN specimens.

4. Conclusion

In this study, the change in microstructure, tensile properties, hardness, and corrosion properties of 201 J1 austenitic stainless steel were investigated after solution nitriding and annealing. The major findings can be concluded as follows:

1. After solution nitriding, large austenite grains with N diffused layer of 300 μm formed below the surface. Cr carbides/carbonitrides formed at the austenite grain boundaries within the N diffused layer. Annealing after solution nitrided, N diffused out of the surface, and a martensite/austenite layer was formed with high concentration of Fe and Cr.
2. The yield and tensile stresses decrease while the elongation increases after solution nitriding because of the increase in grain size. Work hardening behavior was reduced as TRIP behavior disappeared due to the increase in the mechanical stability of austenite from the increase in N content.
3. Annealing the solution nitrided specimen decreases yield stress due to the further increases in austenite grain size. Elongation significantly decreased with fracture resembled brittleness without necking. The hardening behavior was similar to the as-received specimen, in which TRIP behavior was shown. The lack of necking behavior was due to the formation of brittle martensite/austenite layer at the surface, which could promote crack initiation during tensile test.
4. The hardness of the solution nitrided specimen near the surface was slightly increased due to the existence of N diffused layer compared to the center area. Austenite grain boundaries in N diffused layer were significantly higher than the average values, caused by the presence of small carbides/carbonitrides particles.
5. The specimen annealed after solution nitriding shows decreased hardness at the inside area compared to before annealing, as the austenite grain size increased and N content was decreased due to the outward diffusion. The layer showed high hardness at the top surface and low hardness underneath, representing martensite and austenite, respectively. The high hardness spots at austenite grain boundaries were not present, confirming the dissolution of carbide/carbonitride particles.
6. The corrosion resistance of 201 J1 austenitic stainless steel was enhanced by solution nitriding due to the existence of diffused nitrogen layer, despite the formation of Cr-carbide/carbonitride particles at grain boundary. By annealing the solution nitrided specimens, corrosion resistance was further improved due to the formation of a high-Cr layer on the surface and the dissolution of carbide/carbonitride particles.

Acknowledgement

This research was financially supported by the Faculty of Engineering, Chulalongkorn University. The authors would like to express their gratitude to Posco-Thainox Public Co., Ltd. for providing the test materials, and to Thai Tohken Thermo Co., Ltd. for supporting the heat treatment and supplying experimental equipment.

References

[1] A. F. Padilha, R. L. Plaut, and P. R. Rios, "Annealing of cold-worked austenitic stainless steels," *ISIJ international*, vol. 43, no. 2, pp. 135–143, 2003.

[2] M. Talha, C. K. Behera, and O. P. Sinha, "A review on nickel-free nitrogen containing austenitic stainless steels for biomedical applications," *Materials Science and Engineering: C*, vol. 33, no. 7, pp. 3563–3575, 2013.

[3] A. Pardo, M. C. Merino, A. E. Coy, F. Viejo, R. Arrabal, and E. Matykina, "Pitting corrosion behaviour of austenitic stainless steels–combining effects of Mn and Mo additions," *Corrosion Science*, vol. 50, no. 6, pp.1796–1806, 2008.

[4] S. S. M. Tavares, J. M. Pardal, M. G. Da Silva, H. F. G. D. Abreu, and M. R. Da Silva, "Deformation induced martensitic transformation in a 201 modified austenitic stainless steel," *Materials characterization*, vol, 60, no. 8, pp. 907–911, 2009.

[5] M. Metikoš-Huković, R. Babić, Z. Grubač, Ž. Petrović, and N. Lajçi, "High corrosion resistance of austenitic stainless steel alloyed with nitrogen in an acid solution," *Corrosion science*, vol. 53, no. 6, pp. 2176–2183, 2011.

[6] L. Mosecker, D. T. Pierce, A. Schwedt, M. Beighmohamadi, J. Mayer, W. Bleck, and J. E. Wittig, "Temperature effect on deformation mechanisms and mechanical properties of a high manganese C^+ N alloyed austenitic stainless steel," *Materials Science and Engineering: A*, vol. 642, pp. 71–83, 2015.

[7] N. Saenarjhan, J. H. Kang, and S. J. Kim, "Effects of carbon and nitrogen on austenite stability and tensile deformation behavior of 15Cr-15Mn-4Ni based austenitic stainless steels," *Materials Science and Engineering: A*, vol. 742, pp. 608–616, 2019.

[8] J. Alphonsa, V. S. Raja, and S. Mukherjee, "Study of plasma nitriding and nitrocarburizing for higher corrosion resistance and hardness of 2205 duplex stainless steel," *Corrosion Science*, vol. 100, pp. 121–132, 2015.

[9] M. Nakajima, Y. Nakamura, K. Suzuki, Y. Bai, and Y. Uematsu, "Effect of solution treatment after nitriding on fatigue properties in type 304 stainless steel," *International Journal of Fatigue*, vol. 68, pp. 103–110, 2014.

[10] M. Tsujikawa, N. Yamauchi, N. Ueda, T. Sone, and Y. Hirose, "Behavior of carbon in low temperature plasma nitriding layer of austenitic stainless steel," *Surface and Coatings Technology*, vol. 193, no. 1–3, pp. 309–313, 2005.

[11] V. H. Baggio-Scheid, A. J. Abdalla, and G. De Vasconcelos, "Effect of heating post-treatment on nitrided stainless steel," *Surface and Coatings Technology*, vol. 201, no. 7, pp. 4058–4061, 2006.

[12] T. Nakanishi, T. Tsuchiyama, H. Mitsuyasu, Y. Iwamoto, and S. Takaki, "Effect of partial solution nitriding on mechanical properties and corrosion resistance in a type 316L austenitic stainless steel plate," *Materials Science and Engineering: A*, vol. 460–461, pp. 186–194, 2007.

[13] H. Mitsui, and S. Kurihana, "Solution nitriding treatment of Fe–Cr alloys under pressurized nitrogen gas," *ISIJ International* vol. 47, no. 3, pp. 479–485, 2007.

[14] T. Tsuchiyama, S. Takaki, H. Ito, and K. Kataoka, "Fabrication of ultrahigh nitrogen austenitic steels by nitrogen gas absorption into solid solution," *Metallurgical and materials transactions A*, vol. 34, pp. 2591–2599, 2003.

[15] D. Kuroda, T. Hanawa, T. Hibaru, S. Kuroda, M. Kobayashi, and T. Kobayashi, "New manufacturing process of nickel-free austenitic stainless steel with nitrogen absorption treatment," *Materials Transactions*, vol. 44, no. 3, pp. 414–420, 2003.

[16] M. H. S. M. Hernandez, M. H. Staia, and E. S. Puchi-Cabrera, "Evaluation of microstructure and mechanical properties of nitrided steels," *Surface and Coatings Technology*, vol. 202, no. 10, pp. 1935–1943, 2008.

[17] L. Shen, L. Wang, Y. Wang, and C. Wang, "Plasma nitriding of AISI 304 austenitic stainless steel with pre-shot peening," *Surface and Coatings Technology*, vol. 204, no. 20, pp. 3222–3227, 2010.

[18] Y. Sun, and T. Bell, "Low temperature plasma nitriding characteristics of precipitation hardening stainless steel," *Surface Engineering*, vol. 19, no. 5, pp. 331–336, 2003.

[19] B. Weiss, and R. Stickler, "Phase instabilities during high temperature exposure of 316 austenitic stainless steel," *Metallurgical and Materials Transactions B*, vol. 3, pp. 851–866, 1972.

[20] K. Hirota, K. Mitani, M. Yoshinaka, and O. Yamaguchi, "Simultaneous synthesis and consolidation of chromium carbides (Cr_3C_2, Cr_7C_3 and $Cr_{23}C_6$) by pulsed electric-current pressure sintering," *Materials Science and Engineering: A*, vol. 399, no. 1–2, pp. 154–160, 2005.

[21] T. Thomberg, H. Kurig, A. Jänes, and E. Lust, "Mesoporous carbide-derived carbons prepared from different chromium carbides," *Microporous and mesoporous materials*, vol. 141, no. 1–3, pp. 88–93, 2011.

[22] Y. Gao, and S. Zheng, "Effect of plasma nitriding temperatures on characteristics of AISI 201 austenitic stainless steel," *Surface Review and Letters*, vol. 23, no. 01, p.1550084, 2016.

[23] X. Tao, J. Gu, and L. Han, "Carbonitride dissolution and austenite grain growth in a high Cr ferritic heat-resistant steel," *ISIJ international*, vol. 54, no. 7, pp. 1705–1714, 2014.

[24] T. Masumura, N. Nakada, T. Tsuchiyama, S. Takaki, T. Koyano, and K. Adachi, "The difference in thermal and mechanical stabilities of austenite between carbon-and nitrogen-added metastable austenitic stainless steels," *Acta Materialia*, vol. 84, pp. 330–338, 2015.

[25] T. H. Lee, E. Shin, C. S. Oh, H. Y. Ha, and S. J. Kim, "Correlation between stacking fault energy and deformation microstructure in high-interstitial-alloyed austenitic steels," *Acta Materialia*, vol. 58, no. 8, pp. 3173–3186, 2010.

[26] J. Y. Lee, J. S. Hong, S. H. Kang, and Y. K. Lee, "The effect of austenite grain size on deformation mechanism of Fe–17Mn steel," *Materials Science and Engineering: A*, vol. 809, p. 140972, 2021.

[27] A. Kisko, R. D. K. Misra, J. Talonen, and L. P. Karjalainen, "The influence of grain size on the strain-induced martensite formation in tensile straining of an austenitic 15Cr–9Mn–Ni–Cu stainless steel," *Materials Science and Engineering: A*, vol. 578, pp. 408–416, 2013.

[28] R. Zhou, D. O. Northwood, and C. Liu, "On nitrogen diffusion during solution treatment in a high nitrogen austenitic stainless steel," *Journal of Materials Research and Technology*, vol. 9, no. 2, pp. 2331–2337, 2020.

[29] Q. Ran, Q. Liu, Y. Xu, W. Xu, J. Li, X. Xiao, J. Hu, and L. Jiang, "Nitrogen-induced selective high-temperature internal oxidation behavior in duplex stainless steels 19Cr–10Mn–0.3 Ni–xN," *Corrosion Science*, vol. 98, pp. 737–747, 2015.

[30] M. Soleimani, A. Kalhor, and H. Mirzadeh, "Transformation-induced plasticity (TRIP) in advanced steels: A review," *Materials Science and Engineering: A*, vol. 795, p. 140023, 2020.

[31] Z. Zeng, J. Zhao, X. Luo, G. Yang, and H. Yin, "Study on mechanical properties and deformation mechanism of TWIP stainless steel," *Metals*, vol. 12, no. 9, p. 1436, 2022.

[32] E. I. Galindo-Nava, and P. E. J. Rivera-Díaz-del-Castillo, "Understanding martensite and twin formation in austenitic steels: A model describing TRIP and TWIP effects," *Acta Materialia*, vol. 128, pp. 120–134, 2017.

[33] T. Ma, J. Gao, H. Li, C. Li, H. Zhang, and Y. Li, "Microband-induced plasticity in a Nb content Fe–28Mn–10Al–C low density steel," *Metals*, vol. 11, no. 2, p. 345, 2021.

[34] C. Tromas, J. C. Stinville, C. Templier, and P. Villechaise, "Hardness and elastic modulus gradients in plasma-nitrided 316L polycrystalline stainless steel investigated by nanoindentation tomography," *Acta Materialia*, vol. 60, no. 5, pp. 1965–1973, 2012.

[35] S. Münstermann, Y. Feng, and W. Bleck, "Influencing parameters on elastic modulus of steels," *Canadian Metallurgical Quarterly,* vol. 53, no. 3, pp. 264–273, 2014.

[36] D. M. Field, D. S. Baker, and D. C. Van Aken, "On the prediction of α-martensite temperatures in medium manganese steels," *Metallurgical and Materials Transactions A*, vol. 48, pp. 2150–2163, 2017.

[37] H. Y. Yu, "Variation of elastic modulus during plastic deformation and its influence on springback," *Materials & Design*, vol. 30, no. 3, pp. 846–850, 2009.

[38] G. Niu, H. Wu, D. Zhang, N. Gong, and D. Tang, "Heterogeneous nano/ultrafine-grained medium Mn austenitic stainless steel with high strength and ductility," *Materials Science and Engineering: A*, vol. 725, pp. 187–195, 2018.

[39] G. Chen, R. Rahimi, G. Xu, H. Biermann, and J. Mola, "Impact of Al addition on deformation behavior of Fe–Cr–Ni–Mn–C austenitic stainless steel," *Materials Science and Engineering: A*, vol. 797, p. 140084, 2020.

[40] E. I. Galindo-Nava, and P. E. J. Rivera-Díaz-del-Castillo, "Understanding the factors controlling the hardness in martensitic steels," *Scripta Materialia*, vol. 110, pp. 96–100, 2016.

[41] Y. Yu, S. Shironita, K. Souma, and M. Umeda," Effect of chromium content on the corrosion resistance of ferritic stainless steels in sulfuric acid solution," *Heliyon*, vol. 4, no. 11, p. e00958, 2018.

[42] J. K. Kim, Y. H. Kim, J. S. Lee, and K. Y. Kim, "Effect of chromium content on intergranular corrosion and precipitation of Ti-stabilized ferritic stainless steels," *Corrosion Science*, vol. 52, no. 5, pp. 1847–1852, 2010.